Real-Time SAXS Observations of Lamella-Forming Block Copolymers under Large Oscillatory Shear Deformation†

Shigeru Okamoto,‡ Kenji Saijo, and Takeji Hashimoto*

Division of Polymer Chemistry, Graduate School of Engineering, Kyoto University, Kyoto 606, Japan

Received December 21, 1993®

ABSTRACT: Real-time and in-situ small-angle X-ray scattering (SAXS) studies were conducted on polystyrene-*block*-poly(ethylene-*alt*-propylene) copolymer films having alternating lamellar microdomains. SAXS was detected with a 2D detector from the film specimens subjected to a large-amplitude oscillatory shear deformation with a sawtooth type strain γ ($-0.5 \leq \gamma \leq 0.5$) at frequency f = 0.0149 or 1 Hz and at temperature T = 105 or 130 °C. The specimens initially had a uniaxial orientation with the lamellar normal **l** preferentially oriented parallel to the film normal (OZ axis). The shear deformation at low temperature and low frequency (f = 0.0149 Hz, T = 105 °C) or that at high temperature and high frequency (f = 1 Hz, T = 130 °C), with the displacement vector parallel to the OY axis and the shear gradient axis parallel to the OZ axis, gave a biaxial orientation with **l** preferentially oriented along either the OZ or OY axis, the former being dominant to the latter. On the other hand, the shear deformation at high temperature and low frequency (f = 0.0149 Hz, T = 130 °C) gave an improved uniaxial orientation of **l** with respect to the OZ axis. A preferred orientation of **l** along the OX axis, the neutral axis, was not detected in any case. The two deformations which gave the biaxial orientation involved about the same shear stress level, but this stress level was much higher than that involved in the deformation giving rise to the improved uniaxial orientation.

I. Introduction

Investigation of the self-assembly of block copolymers (self-assembling processes and mechanisms, and structures self-assembled in equilibrium or nonequilibrium) provides a fascinating research theme in statistical mechanics of complex fluids. The investigation is important also from a viewpoint of controlling "nanopattern", as the copolymers can form ordered patterns of a nanometer scale. Most of the works along this line so far have been done for the copolymer systems without applied fields.[1,2] An extension of the above studies for the systems subjected to applied fields provides a theme one-step advanced; it involves intriguing problems on open, nonequilibrium systems. Steady-state or transient nanopatterns developed are expected to be extremely rich in their varieties.

The effect of flow on such nanopatterns as lamellar and cylindrical morphologies was first demonstrated by Keller et al.[3] They showed it gives rise to highly aligned lamellae or cylinders for polystyrene-*block*-polybutadiene-*block*-polystyrene (SBS) copolymer melts. Subsequently, Hadzioannou et al.[4] obtained comparable results with polystyrene-*block*-polyisoprene (SI) and polystyrene-*block*-polyisoprene-*block*-polystyrene (SIS) using oscillatory shear deformation. These studies were extended to detailed studies on the deformation behavior of the block copolymer microdomains as studied by TEM, SAXS, and birefringence.[5,6] More recently, there have been many experimental reports published on the shear-induced orientation of cylindrical[7-11] and lamellar microdomains.[12,13] The shear effects are also discussed on lattice orientation and deformation of the spherical microdomains.[14,15] The shear affects the phase transition also, as reported on the shear-induced disorder-to-order transition.[16,17]

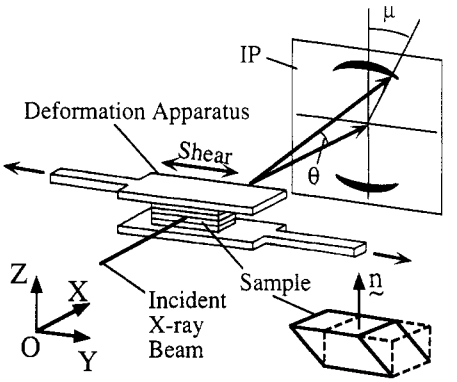

Figure 1. Optical setup of the SAXS apparatus used in this work where an imaging plate (IP) was used as a 2D detector. The Cartesian coordinate $OXYZ$ is defined such that OX and OZ are parallel to the incident X-ray beam and the vertical direction of the apparatus, respectively, except for Figure 11 in which the beam was irradiated along OX, OY, and OZ. A sawtooth type large-amplitude oscillatory shear deformation with a frequency of 0.0149 or 1 Hz is imposed with the shear displacement vector parallel to the OY axis. The unit vector **n** normal to the specimen surfaces is set normal to the OXY plane. θ and μ are a scattering angle and an azimuthal angle, respectively.

In this work we focus on the effect of large-amplitude oscillatory shear deformation on orientations of lamellar microdomains developed in a polystyrene-*block*-poly(ethylene-*alt*-propylene) diblock copolymer (SEP). The effect of shear deformation or flow on the lamellar microdomains was previously reported by Koppi et al.[12] and Winey et al.[13] They reported the unique "perpendicular orientation" of lamellae under the reciprocating shear deformation at high frequencies and at temperatures (T) close to but below the order–disorder transition (ODT) temperature (T_{ODT}) or the normal "parallel orientation" of lamellae at the same T but at low frequencies or at T far below T_{ODT} irrespective of frequencies. The perpendicular orientation shows the lamellar normals **l** preferentially oriented parallel to the neutral axis of the shear deformation (OX axis), while the parallel orientation shows **l** preferentially oriented parallel to the shear gradient direction (OZ axis) (see Figure 1). Koppi et al. reported

* To whom correspondence should be addressed.

† Presented in part at the 39th Annual Meeting of the Society of Polymer Science, Kyoto, Japan, May 1990 [*Polym. Prepr. Jpn., Soc. Polym. Sci. Jpn.* **1991**, *39* (No. 3), 384] and at the 39th Annual Meeting of the Society of Polymer Science, Nagoya, Japan, Oct 1990; *Polym. Prepr. Jpn., Soc. Polym. Sci. Jpn.* **1991**, *39* (No. 10), 3563–3565].

‡ Present address: Department of Materials Science and Engineering, Nagoya Institute of Technology, Nagoya 466, Japan.

® Abstract published in *Advance ACS Abstracts*, August 15, 1994.

0024-9297/94/2227-5547$04.50/0

the experiments at T = 356 K for a PEP–PEE block copolymer having T_{ODT} = 369 K (T/T_{ODT} = 0.97 or χ_{ODT}/χ = 0.98) or at T = 423 K for a copolymer having T_{ODT} = 564 K (T/T_{ODT} = 0.75 or χ_{ODT}/χ = 0.78), while Winey et al. reported the experiments at T = 371 and 417 K for a SI diblock copolymer having T_{ODT} = 425 K, corresponding to T/T_{ODT} = 0.87 or χ_{ODT}/χ = 0.79 and T/T_{ODT} = 0.98 or χ_{ODT}/χ = 0.97, respectively.

In this paper we aim to report a new class of information on the effects of large-amplitude shear deformation on a lamellar orientation: shearing at a low temperature or in an even high segregation regime develops a *biaxial orientation* of lamellae as shown in Figure 10. It is also important to note that all our SAXS data, except those shown in Figure 11, were obtained *in situ* during the shear deformation and during relaxation upon cessation of shear, whereas previous works reported[12,13] were not done *in situ*, involving additional processes such as cooling, cutting, and mounting the sample specimens having been subjected to the shearing at a given T and frequency f for the SAXS and SANS (small-angle neutron scattering) experiments. Only a few scattering experiments[10,15–17] have been carried out *in situ*, despite the necessity of doing the *in situ* experiments to avoid any artifacts encountered by the additional processes. Here we shall report some of our initial experimental results, especially anomalous biaxial orientation of lamellae. The detailed interpretation of the reorientation mechanism will be left as a future work.

II. Experimental Methods

A. Specimen. The SEP sample was kindly supplied from Kurare Co., Ltd., Japan. It was prepared by selective hydrogenation[18] of the polyisoprene block of a precursor SI diblock copolymer prepared by living anionic polymerization. It has a number-average molecular weight $\bar{M}_n = 3.2 \times 10^4$, a heterogeneity index $\bar{M}_w/\bar{M}_n$ = 1.5 where $\bar{M}_w$ is the weight-average molecular weight, and a weight fraction of PS of 0.37. The polyisoprene block before hydrogenation had a microstructure rich in 1,4-linkage (95%). Film specimens were prepared by the solution-cast method with toluene as a solvent, with 5% polymer solution being used. The films thus obtained were dried under vacuum at 30 °C until a constant weight was attained and subsequently annealed at 30 °C for 2 days, prior to use for real-time and *in situ* studies.

B. Dynamic SAXS Apparatus. The small-angle X-ray scattering (SAXS) apparatus used in this work is comprised of a 12-kW rotating-anode X-ray generator operated at 50 kV and 200 mA, with Cu Kα radiation (λ = 1.54 Å) monochromatized with a flat graphite crystal, a 1.7-m camera with a point source image and pinhole collimation, and an imaging plate (IP) as a 2D detector at about 1410 mm from the sample center. Two pairs of guard slits were placed between the sample position and the second pinhole to avoid parasitic scattering from the pinholes. The details of the IP which was designed in our laboratory for time-resolved SAXS studies will be reported elsewhere.[19] The Cartesian coordinate $OXYZ$ is defined such that the OX and OZ axes are parallel to the incident X-ray beam and the vertical direction of the apparatus, respectively.

The oscillatory shear strain was imposed on the film specimens as shown in Figure 1. The specimen was subjected to a large amplitude of sawtooth type shear strain γ with amplitude γ_0 = 50% and frequency f = 0.0149 or 1 Hz at a temperature T = 105 or 130 °C (γ varies between $\pm\gamma_0$). The specimen surfaces are set parallel to the OXY plane with the specimen normal **n** parallel to the OZ axis and sandwiched between two metal plates with the shear displacement direction along OY axis. Unless otherwise stated, the incident X-ray beam was irradiated parallel to the OX axis and the shear strain $\gamma = dy/dz$ existed in the plane OYZ. The oscillatory deformation was driven by a hydraulic deformation apparatus whose details on the computer-controlled data acquisitions and the machine operations were given elsewhere.[15,20] We employed the graphic enhancement technique for 2D SAXS patterns[21] in order to facilitate a visual inspection of their higher order maximum intensity distributions with respect to an azimuthal angle μ also defined in Figure 1.

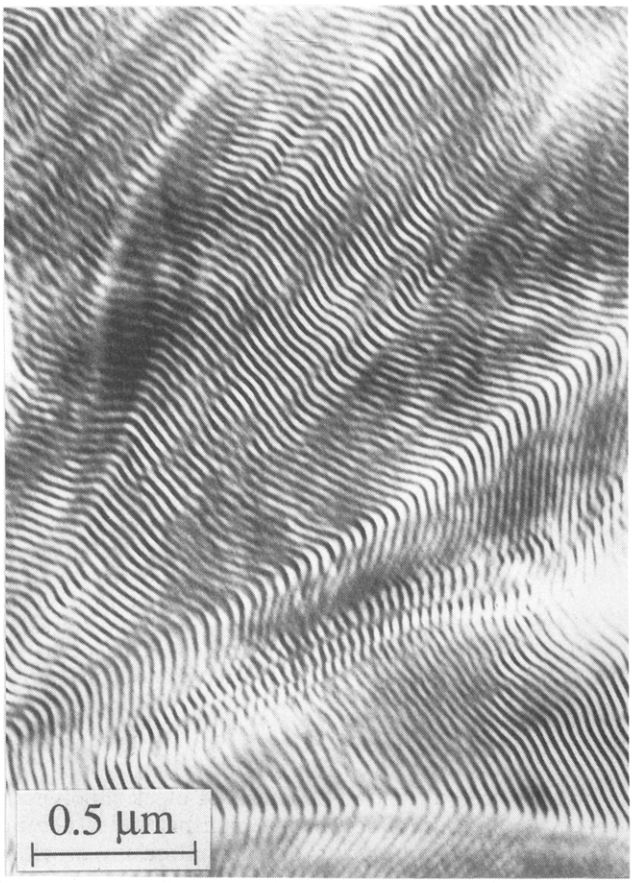

Figure 2. Typical TEM micrograph for undeformed SEP specimens ultramicrotomed and stained with RuO_4. The micrograph shows the grain structure whose grain-boundary structure is given by Scherk's first surface.

C. TEM Observation. Transmission electron microscopy (TEM) was conducted on the ultrathin sections of ca. 50 nm sliced from the specimen using a Reichert-Jung Ultracut E with a cryogenic unit FC 4E. The thin sections were picked up on 400-mesh copper grids and stained with ruthenium tetraoxide (RuO_4) vapor prepared by the method reported by Montezinos et al.[22] TEM was performed at 100 kV with a Hitachi H-600 using a rotating specimen holder.

D. Mechanical Properties. Dynamic mechanical properties and stress relaxation of the specimens were measured by RDS 7700-II, Rheometrics Co., Ltd.

III. Experimental Results

A. Characterization of the Undeformed State. Figure 2 shows a typical TEM micrograph obtained from the SEP specimens. It shows a mosaic structure consisting of grains of lamellar microdomain with different orientation. The bright phase corresponds to the microdomains composed of poly(ethylene-*alt*-propylene) block chains (PEP), while the dark phase corresponds to that of polystyrene block chains (PS) selectively stained by RuO_4. This specimen contains a numerous number of grain boundaries with various types of interesting TEM images, whose details were analyzed and discussed elsewhere[23] for a similar SEP system showing the lamellar microdomain morphology.

An average grain size is roughly estimated as follows. The size of the grain parallel to the lamellar interface, i.e., the average span of the straight lamellae, is a few micrometers, while the size of the grain normal to the lamellar interface is several times larger than this. Our

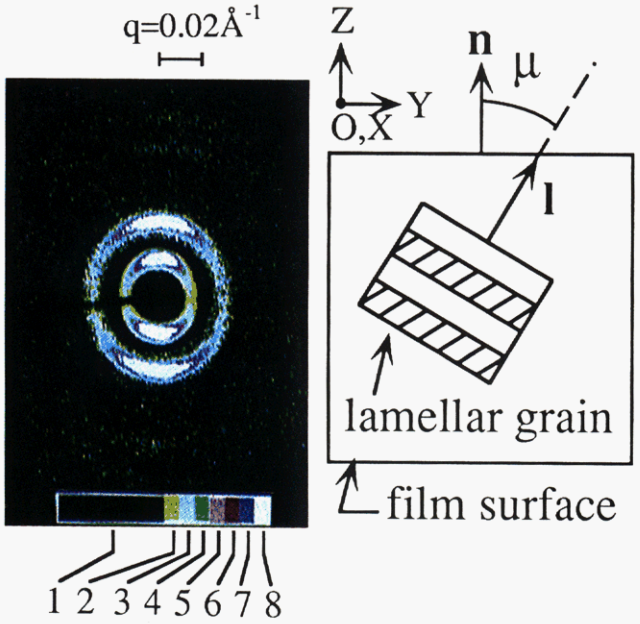

Figure 3. 2D SAXS pattern for undeformed SEP specimens. **n** and **l** are unit vectors parallel to the film normal and lamellar normal, respectively. Note that a direct-beam stopper interferes with the left half of the pattern in the near equatorial direction, giving rise to an abrupt intensity drop along the scattering ring. The same effect is seen also in Figure 8. The intensity ratio of the second-order maximum relative to that of the first-order maximum is approximately 1/15. The eight different colors in the bar, attached at the bottom of the pattern, indicate scattering intensity levels in a linear scale that were used in the graphic enhancement procedure, where each color bar corresponds to each intensity level interval (1–8 correspond to 0–0.61, 0.61–0.67, 0.67–0.72, 0.72–0.78, 0.78–0.83, 0.83–0.89, 0.89–0.94, and 0.94–1.0, relative to the intensity maximum).

analysis indicated that all the grain-boundary images are explained by and large in terms of the minimal surface, designated Scherk's first surface.[24,25] Through this surface, a set of the PS and PEP lamellae with a given orientation is connected smoothly to another set of the corresponding lamellae having a different orientation without intersections of dissimilar lamellae, i.e., the PS (PEP) lamellae in a given set being connected to the PS (PEP) lamellae in another set. Thus the lamellae have 3D continuity through this type of grain boundary.

Figure 3 shows the SAXS pattern for the undeformed specimen, taken with IP using the configuration as indicated in the Cartesian coordinate attached to the figure. The pattern indicates a preferential orientation of the lamellar normals **l** with respect to the film normals **n**. The preferential orientation is more quantitatively shown by the azimuthal angle (μ) dependence of the first-order and the second-order scattering maxima, as shown in Figure 4. Here $\mathcal{I}(\mu)$ designates integrated SAXS intensity distribution as a function of μ, defined by

$$\mathcal{I}(\mu) = \int_{q_1}^{q_2} I(q,\mu)\, q^2\, dq \tag{1}$$

where q_1 and q_2 are the q values at the lower and upper bounds of the first-order maximum or the second-order maximum. If the lamellar normal **l** has a uniaxially symmetric orientation distribution with respect to the film normal, i.e., the OZ axis, its normalized orientation distribution function $N(\mu)$ can be obtained by

$$N(\mu) = \mathcal{I}(\mu)/\int_0^{\pi}\int_{q_1}^{q_2} I(q,\mu)\, q^2 \sin\mu\, dq\, d\mu \tag{2}$$

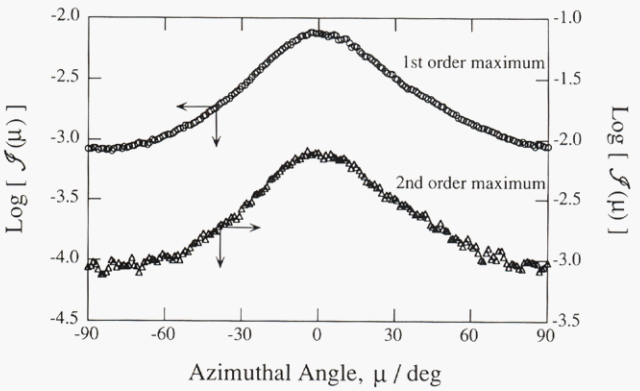

Figure 4. Azimuthal angle (μ) dependence of the first- and second-order diffraction maxima for the pattern shown in Figure 3, with $\mu = 0$ being taken parallel to the OZ axis.

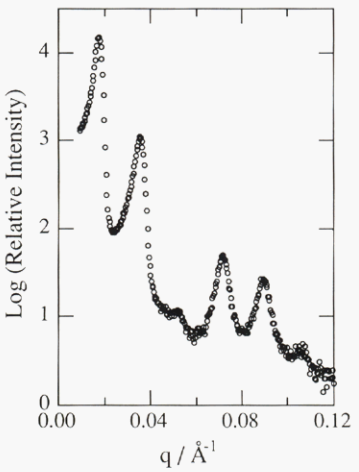

Figure 5. SAXS intensity distribution along the OZ direction in the pattern shown in Figure 3.

The second-order orientation factor f defined by

$$f \equiv [3\langle\cos^2\mu\rangle - 1]/2 \tag{3}$$

can be estimated from $N(\mu)$, i.e.,

$$\langle\cos^2\mu\rangle \equiv \int_0^{\pi}\cos^2\mu N(\mu)\sin\mu\, d\mu \tag{4}$$

The initial state of our sample before shear deformation had the uniaxial orientation of **l** with respect to the OZ axis, and its orientation factor f was estimated to be 0.31 from the data $\mathcal{I}(\mu)$ shown in Figure 4 and from eqs 1–4.

Figure 5 shows the meridional scattering intensity distribution parallel to the film normal as a function of scattering vector $q = (4\pi/\lambda)\sin(\theta/2)$, with θ being the scattering angle. The profile shows multiple-order scattering maxima up to at least the eighth-order maximum, each at the position of integer multiples of the first-order peak position, though the figure includes only up to the sixth-order maximum. This implies a small paracrystalline distortion factor[26] $g = \Delta D/\bar{D} \cong 0.04$ and hence a high regularity in the spatial arrangement of the lamellae. Here ΔD is the standard deviation of the interlamellar spacing D from the mean value $\bar{D} = 35.9$ nm estimated from the Bragg equation $2\bar{D}\sin(\theta/2) = m\lambda$, and m is an integer related to the order of diffraction. The suppression of the third-order maximum is due to the fact that the form factor of the PS lamellae becomes close to zero at the corresponding q value, which yields the volume fraction of the PS lamellae $\phi_{PS} \cong 1/3$. This value is close to the one as calculated from the fraction of PS in SEP on the

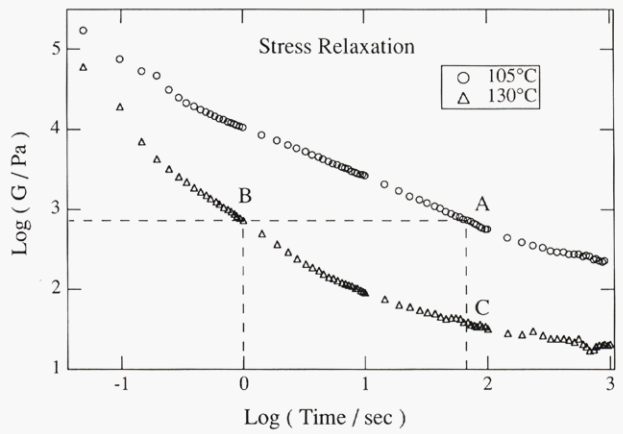

Figure 6. Stress relaxation after a rapid, large shear deformation at 105 and 130 °C. The large deformation of $\gamma = 100\%$ was attained in the time interval of 10 μs.

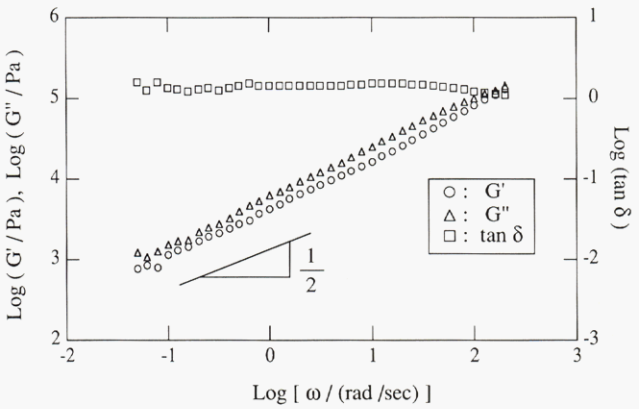

Figure 7. Linear dynamic mechanical response at 130 °C obtained for strain amplitude 1% and static strain 0%.

assumption of complete segregation between PS and PEP ($\phi_{PS} = 0.34$).

B. Mechanical Properties. Figure 6 shows stress relaxation at the two measuring temperatures 105 and 130 °C after rapidly imposing shear strain $\gamma = 100\%$ within 10 μs in which the shear modulus G (Pa) was plotted against t (s) in a double-logarithmic scale. Figure 7 shows linear dynamic mechanical response measured at 130 °C with dynamic strain amplitude 1% and static strain 0% where real and imaginary parts of the shear moduli, G' and G'' respectively, as well as loss tangent tan δ were plotted against angular frequency ω in a double-logarithmic scale. The data at 105 °C were not shown here, but their low-frequency behaviors are the same as those at 130 °C except for a difference in the modulus level. The power-law behaviors of G' and G'' at the low-frequency limit are typical of the ordered microdomains.[8,15,27-30]

C. Effects of Large-Amplitude Oscillatory Shear Deformation. Figure 8 shows effects of the large-amplitude shear deformation at low frequency and at low temperature, i.e., $f = 0.0149$ Hz and $T = 105$ °C. Pattern a was taken *in situ* at 105 °C before the shear deformation, while patterns b and c were taken *in situ* during the deformation, in the deformation cycles N between 1 and 15 and between 75 and 89, respectively. One cycle corresponds to 67 s. On the other hand, patterns d and e were obtained between 0 and 1000 s and between 3000 and 4000 s, respectively, after cessation of shear, with the specimen having been subjected to the 89-cycle oscillatory deformation, i.e., the specimen giving rise to pattern c. A main change of the pattern appears to occur for the first 1000 s after the oscillatory deformation being imposed,

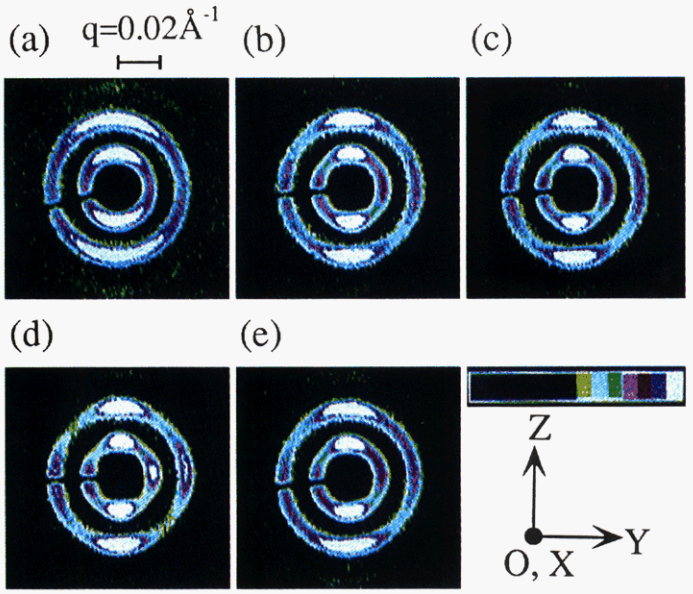

Figure 8. Effects of the large-amplitude oscillatory shear deformation at 0.0149 Hz and 105 °C on the SAXS patterns; (a) pattern for the undeformed specimen at 105 °C; (b and c) patterns taken *in situ* during oscillation cycles N = 1–15 and 75–89, respectively; (d and e) patterns taken *in situ* at 105 °C in the time interval of 0–1000 and 3000–4000 s after cessation of the shear deformation at $\gamma = 0$, respectively, from the state corresponding to that for pattern c. The intensity ratio of the second-order maximum relative to that of the first-order maximum in the meridional direction is approximately 1/10. The eight different colors in the bar attached at the bottom of the pattern indicate scattering intensity levels in a linear scale that were used in the graphic enhancement procedure. Here the lower 60% of the intensity is represented by black, and the upper 40% is equally divided by 7 and represented by seven different colors, each having intensity 0–0.61, 0.61–0.67, 0.67–0.72, 0.72–0.78, 0.78–0.83, 0.83–0.89, 0.89–0.94, and 0.94–1.0, relative to the intensity maximum. The same color representation of the intensity level was used for Figures 9–11.

i.e., N = 1–15 after the deformation. The pattern obtained between N = 64 and 74 (not shown in the figure) was almost identical to pattern c. Thus pattern c appears to represent the steady-state structure attained.

The effects of the shear on the patterns are seen in the following two main points: (i) The μ-dependence of the intensity shows a **biaxial orientation** of lamellar normals, and (ii) with increasing N, the meridional scattering maxima (or diffraction spots along the OZ axis) have a sharper intensity distribution with respect to μ. The effects can be seen more clearly in Figure 12 later. Patterns d and e will be described later in section III-D. To the best of our knowledge, this evolution of the biaxial orientation was observed for the first time.

Figure 9 shows the effects of the large-amplitude shear deformation at low frequency and at higher temperature, i.e., $f = 0.0149$ Hz and $T = 130$ °C. Pattern a was taken *in situ* at 130 °C before the shear deformation, while pattern b was taken in the time interval between 0 and 1000 s after cessation of shear, at $\gamma = 0$, with the sample having been subjected to the oscillations N = 1–60 (0–4020 s). Pattern c was taken as follows. After pattern b was taken, the specimen was rapidly cooled to 105 °C. The pattern was taken *in situ* at 105 °C in the time interval of 1000–2000 s after the quench from 130 to 105 °C. Pattern c will be described later in section III-D. The pattern obtained *in situ* during the oscillation was similar to that shown in pattern b, except for the fact that the former is slightly broader than the latter in terms of the μ-dependence, due to the dynamical change of the pattern

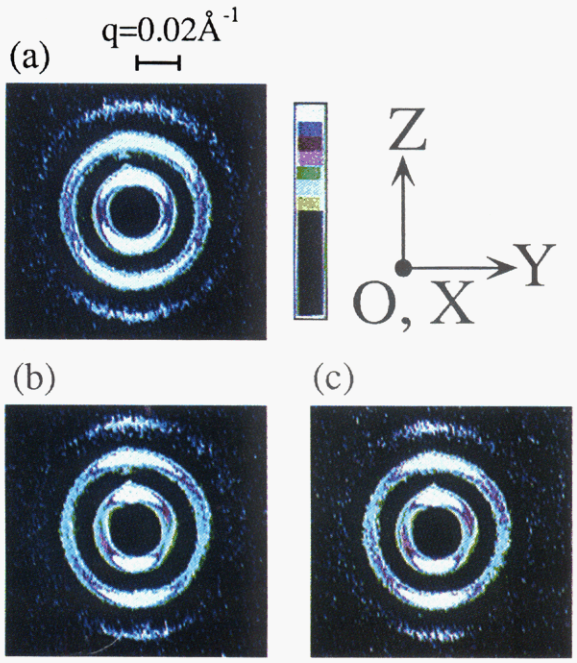

Figure 9. Effects of the large-amplitude oscillatory shear deformation at 0.0149 Hz and at 130 °C on the SAXS patterns: (a) pattern for the undeformed specimen at 130 °C; (b) pattern taken *in situ* at 130 °C in the time interval of 0–1000 after cessation of the oscillatory deformation of $N = 60$ at $\gamma = 0$; (c) pattern taken *in situ* at 105 °C in the time interval of 1000–2000 s after the specimen was first released from strain at 130 °C for 1000 s (pattern shown in part b) and then rapidly cooled to 105 °C. The intensity ratios of the second- and third-order maxima relative to that of the first-order maximum in the meridional direction are approximately 1/10 and 1/500. The eight different colors in the bar are explained in the caption of Figure 8.

induced by the oscillation. The specimen sheared at high temperature gives a sharper uniaxial orientation distribution with the lamellar normals parallel to the *OZ* axis than the undeformed specimen at 130 °C. However, it does not show the biaxial orientation at all. This result is consistent with previous results.[4,12,13] The azimuthal-angle dependence of the patterns will be shown more quantitatively in Figure 15 later.

Figure 10 shows effects of shear deformation at high frequency and at high temperature, i.e., $f = 1$ Hz and $T = 130$ °C. Pattern a was taken *in situ* at 130 °C before the deformation, while pattern b was taken *in situ* during the oscillation of $N = 1$–1000 ($t = 0$–1000 s). Patterns c and d were respectively obtained in the time intervals of 0–1000 and 3000–4000 s after cessation of the oscillatory deformation of $N = 1$–4000. The results will be described in section III-D. The high-frequency oscillation clearly gives rise to a **biaxial orientation** of the lamellar normals in the plane of *OYZ*, clearer than the case of $f = 0.0149$ Hz and $T = 105$ °C.

We next investigate a state of the biaxial orientation of the lamellar normals with respect to the Cartesian coordinate *OXYZ*. Figure 11 shows typical SAXS patterns taken with the incident beam parallel to the *OX* axis [(a) **edge pattern**], *OZ* axis [(b) **through pattern**], and *OY* axis [(c) **end pattern**] for the specimen first deformed at 1 Hz and 130 °C with $N = 1$–4000 and then vitrified by quenching below T_g of the PS domains with liquid nitrogen. The relationship between the Cartesian coordinate and specimen is shown in part d with the *OZ* axis parallel to the film normal **n** and the *OY* axis parallel to the shear displacement vector. Figure 11e shows a model describing the biaxial orientation of the lamellar normals $\mathbf{l}_i$ ($i = 1, 2$) in the specimen with their interfaces oriented parallel to

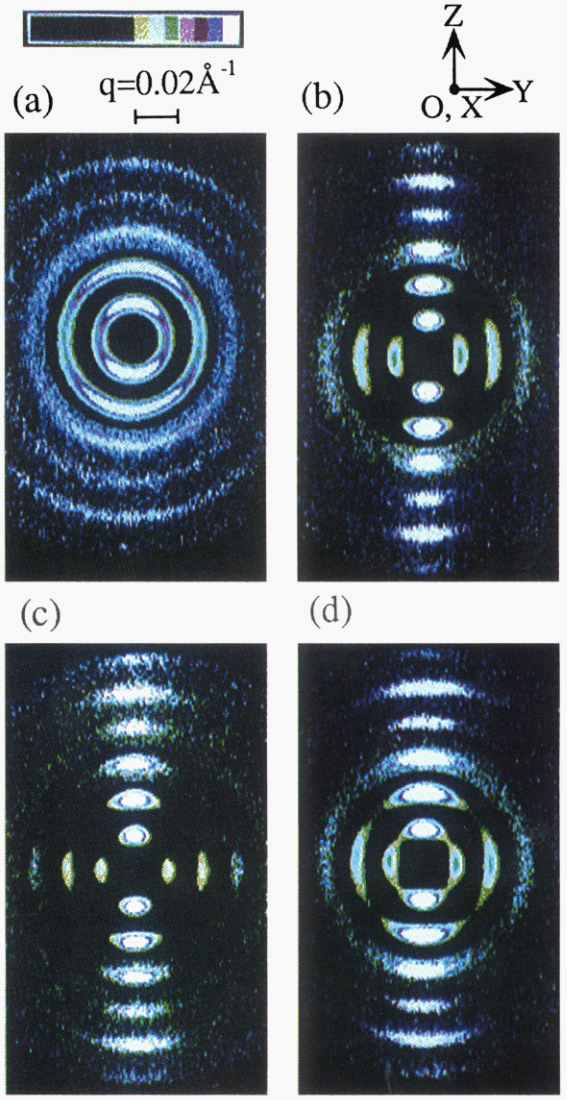

Figure 10. Effects of the large-amplitude oscillatory shear deformation at 1 Hz and at 130 °C on the SAXS patterns: (a) pattern for the undeformed specimen at 130 °C; (b) pattern taken *in situ* during the oscillation cycles $N = 1$–1000; (c and d) patterns taken *in situ* at 130 °C in the time interval of 0–1000 and 3000–4000 s after cessation of the shear deformation, at $\gamma = 0$, respectively, from the state corresponding to that for pattern b. The intensity ratios of the second-, third-, fourth-, and fifth-order maxima relative to that of the first-order maximum in the meridional direction are approximately 1/10, 1/250, 1/1200, and 1/1000. The eight different colors in the bar attached at the top of the pattern are explained in the caption of Figure 8.

either plane *OXY* or *OXZ*. A detailed discussion will be given later in section IV.

D. Relaxation of Orientation after Cessation of Shear. We now describe the change of the patterns shown in Figures 8d,e, 9c, and 10c,d after cessation of shear at $\gamma = 0$. The pattern shown in Figure 8d, obtained right after the cessation, shows a sharper biaxial orientation than the pattern shown in Figure 8c, as is obvious from the sharp minima of the first-order and higher order maxima in the diagonal directions. This primarily reflects the smearing of the biaxiality in pattern c taken *in situ* during the oscillatory deformation, because the four spots (or diffraction maxima) along the *OY* and *OZ* axes move with strain phase during oscillation. The same effect is seen in Figure 10b,c. The change of the lamellar orientation with shearing and that with time after cessation of the imposed shear deformation are more quantitatively seen in the normalized intensity distribution of the first-

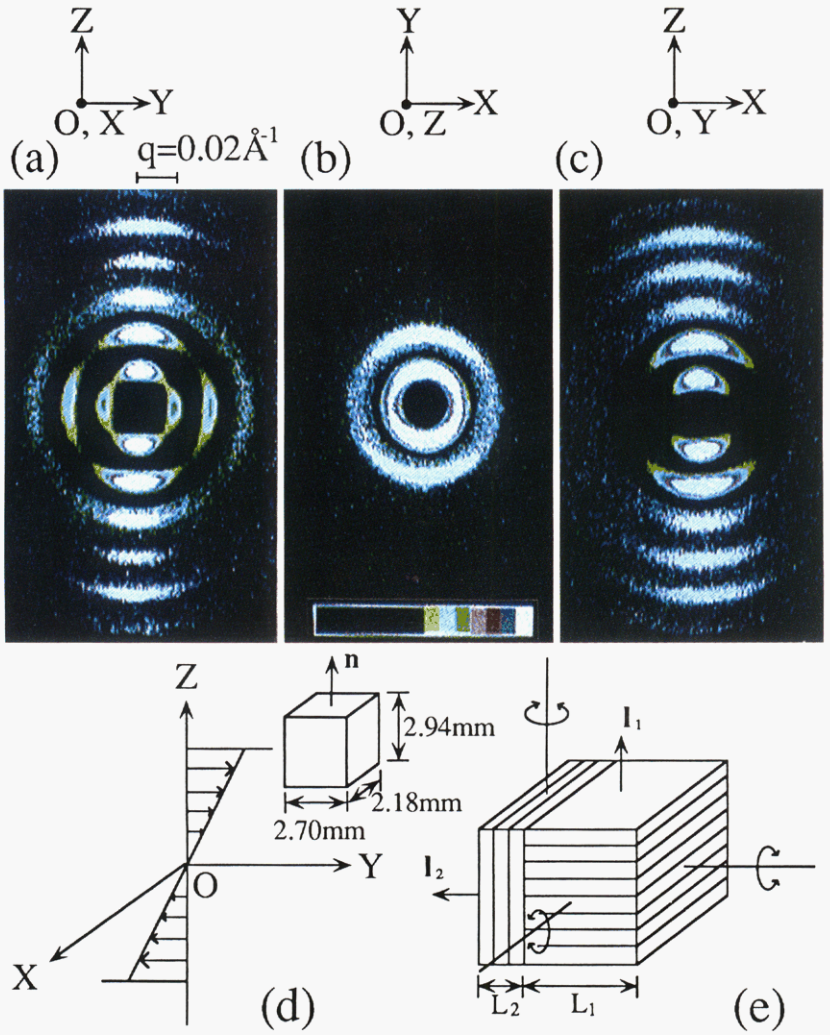

Figure 11. SAXS patterns a–c for the specimens vitrified in the state corresponding to pattern d in Figure 10. The patterns were taken from three directions as specified in part d. Part e represents a model showing the lamellar orientation in the specimen. **n** specifies the film normal, while $\mathbf{l}_1$ and $\mathbf{l}_2$ specify the lamellar normals. The intensity ratios of the second-, third-, fourth-, and fifth-order maxima relative to that of the first-order maximum in the meridional direction are approximately 1/10, 1/500, 1/400, and 1/500 for an edge pattern (pattern a), 1/10, 1/600, 1/600, 1/750 for an end pattern (pattern c), and 1/10 for a through pattern (pattern b). The eight different colors in the bar attached at the bottom of the pattern are explained in the caption of Figure 8.

order scattering maximum $\mathcal{I}(\mu)$ with respect to μ, as shown in Figures 12–15. In these figures $\mu = 0°$ corresponds to the OZ axis parallel to the film normal.

Figure 12 shows the azimuthal-angle dependence of $\mathcal{I}(\mu)$ for patterns a–d in Figure 8, in which curves a–d correspond to $\mathcal{I}(\mu)$ of patterns a–d in Figure 8, respectively. In shearing $\mathcal{I}(\mu)$ changes from curve a to b, indicating the change of the orientation of lamellar normals from a uniaxial to a biaxial orientation. The biaxiality increases slightly from curve b to c, which confirms our observation that the significant change in orientation occurs within the first 15 cycles of the shear. A steady-state biaxial orientation is attained upon further increase of N. The biaxiality is much clearer in curve d than in curve c, due to the absence of the pattern oscillation smearing effect. Comparing patterns d and e in Figure 8, the biaxial orientation developed by the deformation is seen to gradually relax toward a uniaxial orientation after cessation of shear, at $\gamma = 0$, though the biaxiality still remains clearly. An overall orientation of the lamellar normals is also seen to be relaxed. This relaxation behavior is more quantitatively presented in Figure 13.

Figure 13 shows the change of $\mathcal{I}(\mu)$ with time during the relaxation of pattern d to e in Figure 8. Curves 1 and 2 in Figure 13 which respectively correspond to curves a and d in Figure 12 (and hence patterns a and d in Figure 8) were included as a reference. Curve 5 corresponds to pattern e. Thus the change of the pattern from d to e with time during the relaxation is shown in the evolution of $\mathcal{I}(\mu)$ from curve 2 to 5, indicating that the biaxiality decreases with time. The inset of Figure 13 shows the changes of $\mathcal{I}(\mu)$ at $\mu = 0$, 45, and 90° with time where the solid and broken lines indicate a fit of the exponential function $\mathcal{I}(\mu) = A[1 + B \exp(-t/\tau)]$ with the relaxation time $\tau \cong 1.26 \times 10^3$ s, common for all the three curves and $|B|$ is on the order of 0.2–0.7. At the long time limit covered in this experiment, the values $\mathcal{I}(\mu)$ reach almost constant values which still show a slight biaxiality as evident from the fact that $\mathcal{I}(\mu)$ at $\mu = 90°$ is greater than $\mathcal{I}(\mu)$ at $\mu = 45°$.

The orientation relaxation similar to the case shown in Figure 8 is also seen in patterns c and d of Figure 10 obtained for high-frequency and high-temperature deformation. Although the biaxiality is retained even at the longest time of our observation, the orientation distribution of the lamellar normals is clearly seen to become broader with time. Figure 14 shows $\mathcal{I}(\mu)$ where curves a–d respectively correspond to patterns a–d in Figure 10. The same trend as that observed earlier in Figures 12 and 13 is shown, except for the fact that the biaxiality developed (curve c in Figure 14) and the residual biaxiality attained a long time after relaxation of stress (curve d in Figure 14)

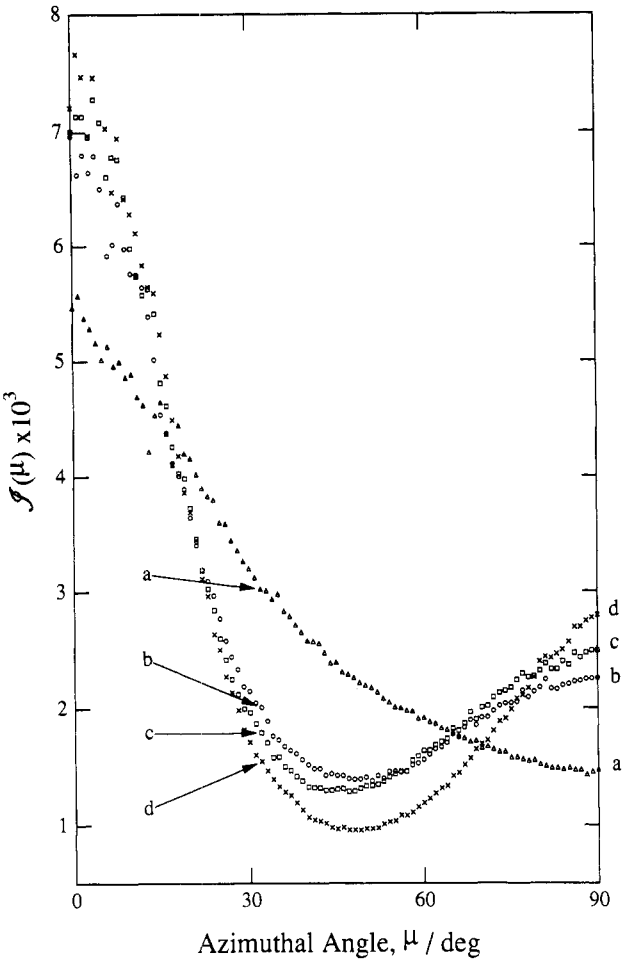

Figure 12. $\mathcal{I}(\mu)$ of the first-order maximum in the SAXS patterns shown in Figure 8, where curves a–d correspond to patterns a–d of Figure 8, respectively. $\mu = 0°$ refers to the vertical direction in the patterns.

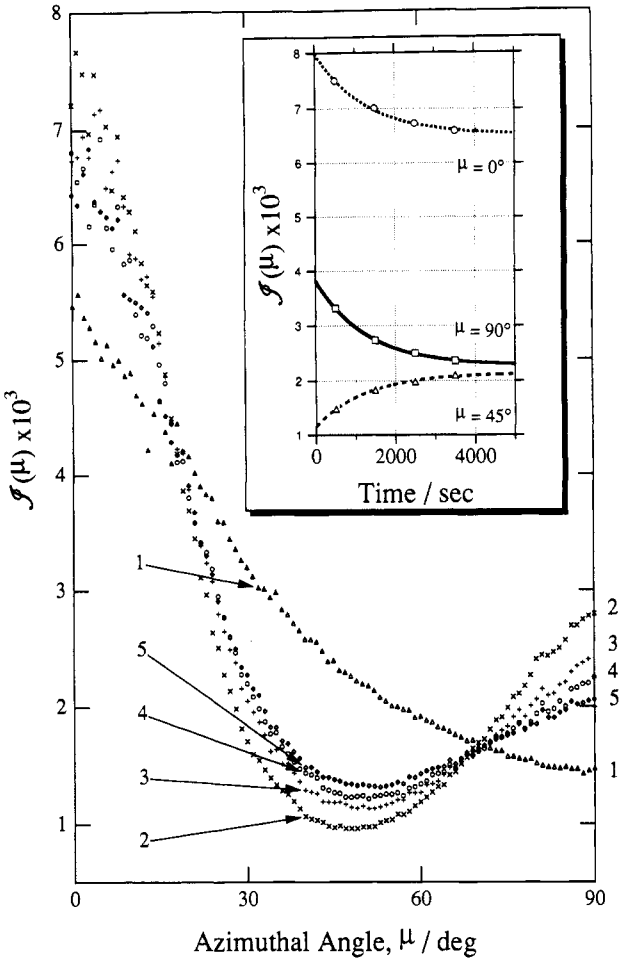

Figure 13. Change of $\mathcal{I}(\mu)$ of the first-order maximum with time during the relaxation of pattern d to e in Figure 8. Curves 1 and 2 in Figure 13, included as a reference, respectively correspond to curves a and d in Figure 12 (and hence to patterns a and d in Figure 8). Curve 5 corresponds to pattern e in Figure 8. $\mu = 0°$ refers to the vertical direction in the patterns. The inset of Figure 13 shows the changes of $\mathcal{I}(\mu)$ at $\mu = 0$, 45, and 90° with time where the solid and broken lines indicate a fitting of the exponential function.

are higher than the corresponding counterparts observed for low-frequency and low-temperature deformation (curves 2 and 5 in Figure 13).

The uniaxial orientation obtained after low-frequency and high-temperature shear deformation (pattern b in Figure 9) did not change at all after cessation of shear at $\gamma = 0$. The patterns taken 1000 s later in the relaxed state at 130 °C were identical to pattern b though they are not shown here. Moreover, the orientation was observed to be unaltered even after this specimen was cooled to 105 °C, as shown in pattern c. These observations are more quantitatively confirmed by the $\mathcal{I}(\mu)$ data shown in Figure 15 where curves a–c respectively correspond to patterns a–c in Figure 9. Although not shown here, all the patterns taken during the time interval up to 3000 s after cooling to 105 °C were the same as that in pattern b or c of Figure 9.

IV. Discussion

It is clearly shown from Figures 10 and 14 that the shear deformation at high frequency and at high temperature ($f = 1$ Hz and $T = 130$ °C) develops a biaxial orientation. The development of the biaxial orientation is also clearly observed for the shear deformation at low frequency and at low temperature ($f = 0.0149$ Hz and $T = 105$ °C) from the μ-dependence of the SAXS pattern shown in Figure 8 and also from curve 2 in Figure 13.

The state of the biaxial orientation attained in the specimen subjected to high-frequency (1 Hz) shear deformation at high temperature (130 °C) cab be investigated from Figure 11. The edge pattern (a) clearly shows a bimodal intensity distribution with respect to an azimuthal angle, with maximum intensity along the OZ and OY axes; the intensity along the OZ axis is stronger than that along the OY axis. The former intensity is attributed to lamellae L_1 with their normals $\mathbf{l}_1$ preferentially oriented along the OZ axis, while the latter intensity is attributed to lamellae L_2 with their normals $\mathbf{l}_2$ preferentially oriented along the OY axis. The fraction of lamellae L_1 should be larger than that of lamellae L_2, judging from the data $\mathcal{I}(\mu)$ shown in Figure 14. The μ-dependence of the SAXS intensity reflects the distributions of $\mathbf{l}_1$ and $\mathbf{l}_2$ in the plane OYZ, i.e., some rotations of L_1 and L_2 around the OX axis.

The through pattern (b) shows a unimodal intensity distribution with respect to an azimuthal angle, with a maximum intensity along the OY axis. This pattern arises also from lamellae L_2 and confirms the biaxial orientation. Its azimuthal breadth depends on an orientation distribution of $\mathbf{l}_2$ in the plane OXY, i.e., some rotations of L_2 around the OZ axis. The end pattern (c) also shows a unimodal intensity distribution with respect to an azimuthal angle, with a maximum intensity along the OZ axis. This pattern arises from lamellar L_1, but its azimuthal breadth reflects an orientation distribution of $\mathbf{l}_1$ in the plane OXZ, i.e., some rotations of L_2 around the OY axis. It may be noted that the intensity along the OY axis in pattern a is not the same as that in pattern b along the OY axis. We interpret

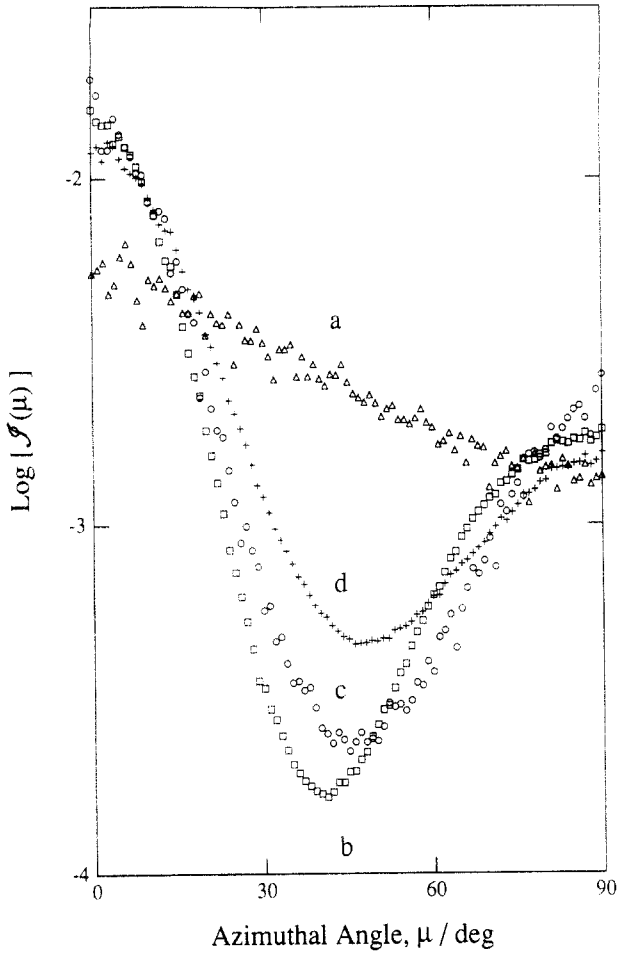

Figure 14. $\mathcal{I}(\mu)$ of the first-order maximum in the patterns shown in Figure 10, where curves a–d correspond to patterns a–d, respectively. $\mu = 0°$ refers to the vertical direction in the patterns.

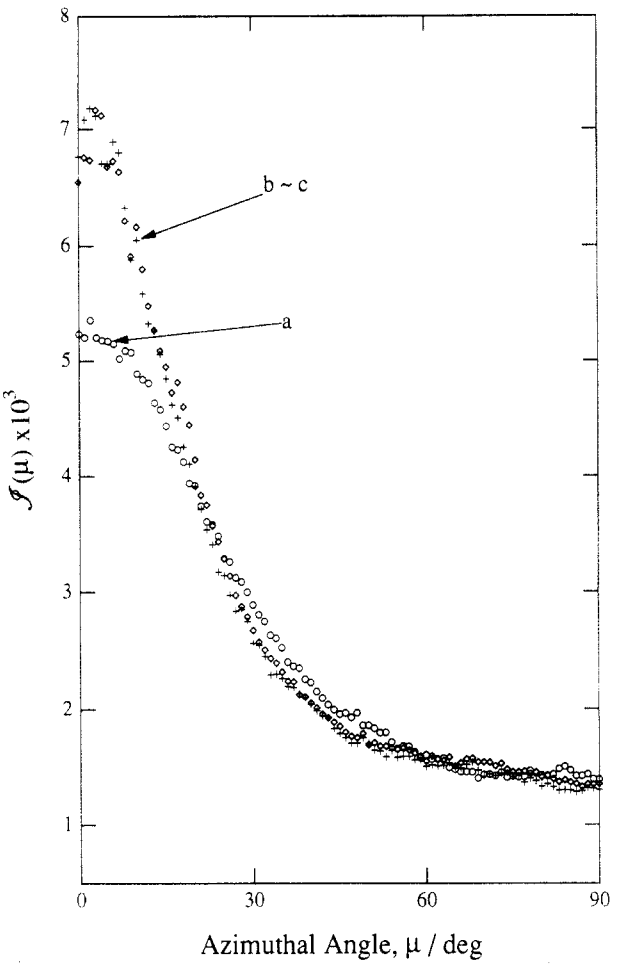

Figure 15. $\mathcal{I}(\mu)$ of the first-order maximum in the patterns shown in Figure 9, where curves a–c correspond to patterns a–c, respectively. $\mu = 0°$ refers to the vertical direction in the patterns.

this as follows. The intensity along the OY axis in pattern a depends on the rotation of the lamellae L_2 around the OZ axis, but the intensity along the OY axis in pattern b depends on the rotation of the lamellae L_2 around the OX axis. Thus the difference in the intensity in a and that in b may be possible if the specimens are composed of many grains and if there is a difference in the degree of the two types of rotation.

In all the cases covered in this work, we cannot find the preferential orientation of the lamellae whose normal vectors are oriented along the OX axis (i.e., **preferential perpendicular orientation**), as reported earlier by Koppi et al.[12] and Winey et al.,[13] although a minor fraction of lamellae has the perpendicular orientation as evident from Figure 11b. Our observation on the lack of preferential perpendicular orientation is not inconsistent with the previous results,[12,13] because our experiments were done far below T_{ODT} and the perpendicular orientation of the lamellae has been observed so far only when shear deformation is applied at T close to T_{ODT}.

Our SEP block copolymer is expected to have very high T_{ODT} which is estimated to be much higher than 400 °C. Hence, the experimental temperatures of 105 and 130 °C are very much far below T_{ODT} and hence our sample is in a very strong segregation regime. The precursor SI diblock copolymer subjected to the selective hydrogenation of a polyisoprene block had T_{ODT} in the melt much higher than 200 °C from SAXS measurements as a function of T. The SAXS measurements of T_{ODT} were done for dioctyl phthalate (DOP) solutions of the SI copolymer as a function of the copolymer concentration ϕ_P. The T_{ODT} values are extrapolated to the value at $\phi_P = 1$ in order to estimate its value in bulk. The T_{ODT} values for the bulk copolymer[31] was 370 ± 20 °C. It is known[32] that SEP has a Flory–Huggins segmental interaction parameter much larger than that of SI. It is thus reasonable to assume T_{ODT} for the SEP specimen used in this work is much higher than 370 °C. Thus our sample has $T/T_{ODT} < 403/643 = 0.63$ and is in an ordered state with a segregation stronger than the lamellae specimens[12,13] previously used. This fast seems to be important for understanding the biaxial orientation behavior. Although the fraction of the lamellae L_2 as shown in Figure 11e is energetically unfavorable under the shear deformation, it may not be possible to be transformed into the parallel lamellae L_1 or into the perpendicular lamellae as reported by Koppi et al. by the processes such as destruction/re-formation[7,9,13] and grain rotation.[7] These processes may be much suppressed under the strong segregation regime. Because the perpendicular lamellae of the type reported by Koppi et al.[12] should be energetically more favorable than the lamellae L_2 under shear deformation, it is puzzling that we cannot attain the biaxial orientation with preferential perpendicular lamellar orientation of the type reported by Koppi et al.

The state of orientation attained by the shear deformation seems to be intimately related to the stress level of our specimens. The biaxial orientation attained either by the low-frequency and low-temperature deformation or by the high-frequency and high-temperature deformation is associated with a higher stress than the uniaxial orientation attained by the low-frequency and high-temperature deformation. This situation may be roughly

seen in the stress relaxation data shown in Figure 6. If we assume that the stress level encountered in an oscillatory deformation with a frequency f is roughly proportional to the relaxation modulus at $t = 1/f$. Then the two deformations giving rise to the biaxial orientation should have almost the same stress level, with their moduli corresponding to point A and B in the figure, while the deformation yielding the uniaxial orientation should have a much lower stress than the above two deformations, with its modulus corresponding to point C.

One last comment we address is that on the stability of the state of orientation attained by the shear deformation. In section III-D it was clarified that the uniaxial orientation attained is quite stable after the cessation of shear. It is also stable at temperatures lower than the temperature of the deformation. Thus the uniaxial orientation appears to be thermodynamically stable or metastable, at least, up to the temperature where the shear deformation is imposed. However, the biaxial orientation attained under the shear deformations employed in this work was shown to relax after cessation as shown in Figures 8 and 10 and Figures 13 and 14. Figures 13 and 14 show quantitatively relaxation of the biaxial orientation toward a uniaxial orientation as well as an overall orientation relaxation, although our data in the long time limit still show a biaxial orientation. Thus the biaxial orientation attained by the shear deformation is a thermodynamically unstable state. However, it certainly exists as a steady state under the shear deformation accompanied by a high stress level, as evident in patterns b and c in Figure 8 and in curves b and c in Figure 12. However, we cannot explain why the biaxial orientation exists in the steady state. This might be associated with the strong segregation phenomenon which suppresses the grain rotation and destruction/re-formation processes as discussed above.

Acknowledgment. This work was supported in part by a Grant-in-Aid for Scientific Research (05453149) from the Ministry of Education, Science and Culture, Japan.

References and Notes

(1) See, for example: Hashimoto, T. In *Thermoplastic Elastomers*; Legge, N. R., Holden, G., Schroeder, H. E., Eds.; Hanser Publishers: Munich Vienna, New York, 1987; p 349.
(2) See, for example: Bates, F. S.; Fredrickson, G. H. *Annu. Rev. Phys. Chem.* **1990**, *41*, 525.
(3) Keller, A.; Pedemonte, E.; Willmouth, F. M. *Kolloid Z. Z. Polym.* **1970**, *238*, 2329; *Nature* **1970**, *225*, 538.
(4) Hadziioannou, G.; Mathis, A.; Skoulios, A. *Colloid Polym. Sci.* **1979**, *257*, 136. Hadziioannou, G.; Picot, C.; Skoulios, A.; Ionescu, M.-L.; Mathis, A.; Duplessix, R.; Gallot, Y.; Lingelser, J.-P. *Macromolecules* **1982**, *15*, 263.
(5) Fujimura, M.; Hashimoto, T.; Kawai, H. *Rubber Chem. Technol.* **1978**, *51*, 215. Hashimoto, T.; Fujimura, M.; Saijo, K.; Kawai, H. *Adv. Chem. Ser.* **1979**, *176*, 257.
(6) Pakula, T.; Saijo, K.; Kawai, H.; Hashimoto, T. *Macromolecules* **1985**, *18*, 1294. Pakula, T.; Saijo, K.; Hashimoto, T. *Macromolecules* **1985**, *18*, 2037.
(7) Morrison, F. A.; Winter, H. H. *Macromolecules* **1989**, *22*, 3533.
(8) Morrison, F. A.; Winter, H. H.; Gronski, W.; Barnes, J. D. *Macromolecules* **1990**, *23*, 4200.
(9) Scott, D. B.; Waddon, A. J.; Lin, Y. G.; Karasz, F. E.; Winter, H. H. *Macromolecules* **1992**, *25*, 4175.
(10) Morrison, F. A.; Mays, J. W.; Muthukmar, M.; Nakatani, A. I.; Han, C. C. *Macromolecules* **1993**, *26*, 5271.
(11) Albalak, R. J.; Thomas, E. L. *J. Polym. Sci., Part B: Polym. Phys.* **1993**, *31*, 37.
(12) Koppi, K. A.; Tirell, M.; Bates, F. S.; Almdal, K.; Colby, R. H. *J. Phys. II (Fr.)* **1992**, *2*, 1941.
(13) Winey, K. I.; Patel, S. S.; Larson, R. G.; Watanabe, H. *Macromolecules* **1993**, *26*, 2542. Winey, K. I.; Patel, S. S.; Larson, R. G.; Watanabe, H. *Macromolecules* **1993**, *26*, 4373.
(14) Almdal, K.; Koppi, K. A.; Bates, F. S. *Macromolecules* **1993**, *26*, 4058.
(15) Okamoto, S.; Saijo, K.; Hashimoto, T. *Macromolecules* **1994**, *27*, 3753.
(16) Koppi, K. A.; Tirrell, M.; Bates, F. S. *Phys. Rev. Lett.* **1993**, *70*, 1449.
(17) Balsara, N. P.; Hammouda, B. *Phys. Rev. Lett.* **1994**, *72*, 360.
(18) Harlan, J. T., Jr. U.S. Patent 3792005, 1974.
(19) Hashimoto, T.; Kume, T.; Saijo, K.; Kimishima, K.; Okamoto, S., in preparation.
(20) Suehiro, S.; Saijo, K.; Ohta, Y.; Hashimoto, T.; Kawai, H. *Anal. Chim. Acta* **1986**, *189*, 41.
(21) Winter, H. H.; Scott, D. B.; Wolfram, G.; Okamoto, S.; Hashimoto, T. *Macromolecules* **1993**, *26*, 7236.
(22) Montezinos, D.; Wells, B. G.; Burns, J. L. *Polym. Lett.* **1985**, *23*, 421.
(23) Nishikawa, Y.; Kawada, H.; Hasegawa, H.; Hashimoto, T. *Acta Polym.* **1993**, *4*, 192.
(24) Nitche, J. C. C. *Lectures on minimal surfaces, volume 1*; Cambridge University Press: Cambridge, U.K., 1989.
(25) Thomas, E. L.; Alward, D. B.; Henkee, C. S.; Hoffman, D. *Nature* **1988**, *334*, 598.
(26) Hashimoto, T.; Nagatoshi, K.; Todo, A.; Hasegawa, H.; Kawai, H. *Macromolecules* **1974**, *7*, 364. Shibayama, M.; Hashimoto, T.; *Macromolecules* **1986**, *19*, 740.
(27) Bates, F. S. *Macromolecules* **1984**, *17*, 2607. Rosedale, J. H.; Bates, F. S. *Macromolecules* **1990**, *23*, 2329. Bates, F. S.; Rosedale, J. H.; Fredrickson, G. H. *J. Chem. Phys.* **1990**, *92*, 6255.
(28) Kawasaki, K.; Onuki, A. *Phys. Rev.* **1990**, *A42*, 3664.
(29) Witten, T. A.; Leibler, L.; Pincus, P. A. *Macromolecules* **1990**, *23*, 824.
(30) Rubinstein, M.; Obukhov, S. P. *Macromolecules* **1993**, *26*, 1740.
(31) Mori, K.; Hashimoto, T., unpublished data.
(32) Owens, J. N.; Gancarz, I. S.; Koberstein, J. T.; Russell, T. P. *Macromolecules* **1989**, *22*, 3380.